

Magnetometry in a diamond anvil cell using nitrogen vacancy centers in a nanodiamond ensemble

Cite as: Rev. Sci. Instrum. 95, 083901 (2024); doi: 10.1063/5.0216877

Submitted: 1 May 2024 • Accepted: 14 July 2024 •

Published Online: 1 August 2024



View Online



Export Citation



CrossMark

David P. Shelton,^{a)}  Waldo Cabriaes, and Ashkan Salamat 

AFFILIATIONS

Department of Physics and Astronomy, University of Nevada, Las Vegas, Nevada 89154-4002, USA

^{a)} Author to whom correspondence should be addressed: shelton@physics.unlv.edu

ABSTRACT

The emerging field of optical magnetometry utilizing negative-charged nitrogen vacancy (NV^-) centers provides a highly sensitive lab bench technique for spatially resolved physical property measurements. Their implementation in high pressure diamond anvil cell (DAC) environments will become common as other techniques are often limited due to the spatial constraints of the sample chamber. Apparatus and techniques are described here permitting for more general use of magnetic field measurements inside a DAC using continuous wave optical detected magnetic resonance in NV^- centers in a layer of nanodiamonds. A microstrip antenna delivers a uniform microwave field to the DAC and is compatible with simple metal gaskets, and the sensor layer of deposited nanodiamonds allows for simple determination of the magnetic field magnitude for B in the 1–100 G range. The ferromagnetic transition in iron at 18 GPa is measured with the apparatus, along with its hysteretic response.

Published under an exclusive license by AIP Publishing. <https://doi.org/10.1063/5.0216877>

I. INTRODUCTION

The negative-charged nitrogen vacancy (NV^-) center in diamond has long been studied for quantum sensor applications due to the combination of several outstanding properties.^{1–6} This work presents an adaptation of the NV^- sensor for the diamond anvil cell. The NV^- center is easily prepared in the $m = 0$ electron spin ground state by optical pumping, and magnetic resonance transfer from the $m = 0$ to the $m = \pm 1$ spin states by an applied microwave (MW) frequency field can be detected optically by a decrease in fluorescence (optically detected magnetic resonance, ODMR). The 2.87 GHz frequency of this resonance is shifted and split by the effects of magnetic field, electric field, temperature, and pressure at the site of the NV^- (2.80 MHz/G, 17 Hz cm/V, -74 kHz/K, and 14.6 MHz/GPa).^{7–12} The diamond host provides mechanical and chemical protection for the NV^- and a magnetically quiet local environment. Zeeman splitting of the $m = \pm 1$ states observed by ODMR provides a sensitive self-calibrated measurement of the applied magnetic field at the NV^- position, and measurements made using a single NV^- center can provide spatial resolution at the nanometer scale. In the following, unless there is risk of confusion with the uncharged NV center,

NV^- will be abbreviated as NV. NV centers are well suited as a sensor inside a diamond anvil cell (DAC). There is good optical access to the extreme environment inside the small sample chamber, and there have been several reports of measurements of pressure^{7,12–15} and magnetic field^{7,16–21} made in a DAC using NV centers, at pressures up to 140 GPa.^{7,21} The apparatus differs in the form of the NV sensor and how the MW field is delivered into the DAC. A single crystal NV diamond sample was used for pressure measurements up to 60 GPa in Ref. 12, and similar NV sensors are 15 μm NV diamond single crystals stuck to the culet¹³ and 1 μm NV diamonds placed¹⁷ or sprinkled^{7,19} or deposited from liquid suspension (drop cast)¹⁴ onto the culet. Alternatively, a NV sensor layer has been implanted 50 nm^{16,21} or 20 nm^{18,20} below the culet surface of the diamond anvil, or both an implanted NV layer and 140 nm NV nanodiamonds were used.¹⁵ MW antennas that have been used are a Pt wire embedded in the insulating gasket or a copper coil wound around the diamond anvil culet,¹² an Au loop antenna on the culet,¹⁵ a W loop antenna deposited on the culet and covered with a 50 μm epitaxial diamond layer,¹³ a Pt foil MW antenna beside and below the gasket on the pavilion of the anvil,¹⁶ a Pt wire,^{7,19,21} a single turn coil on a split gasket,^{18,20} and a 200 μm coil inside the sample chamber.^{14,17}

Diamond anvils with a thin implanted NV layer have the advantage that the sensor layer is protected, spatial resolution is limited only by the optical system, and the orientation of the NV axes is known, but the NV layer will also sense the large stress in the diamond anvil, and special fabrication facilities are required. Depositing NV diamond crystals on the culet is simpler, but the orientation of the crystals is uncontrolled and the potential spatial resolution may be reduced. Problems with current DAC MW antennas are that a straight wire antenna produces a non-uniform field, while a loop antenna may need a split gasket or insulating gasket since the field of the antenna is opposed by the current induced in a conducting gasket. Other MW antennas have been used for NV ODMR sensing outside a DAC.^{4,22–24} The present work describes an ODMR system developed for magnetic field measurements using NV centers in a DAC that addresses some of the issues outlined above. The present implementation uses a NV nanodiamond (NVND) layer as the sensor and a microstrip transmission line for delivering the MW field into the DAC. Magnetic field changes accompanying ferromagnetic or superconducting transitions are most easily measured. The system is demonstrated by measuring the ferromagnetic magnetization change accompanying the pressure-induced transition from α -Fe to ϵ -Fe.

II. MICROSTRIP MICROWAVE ANTENNA

The MW field applied to the thin metal gasket of the DAC in this experiment is polarized with the MW magnetic field parallel to the gasket surface. The solution for a MW field applied on one side of a thin conducting sheet containing a hole, with the MW magnetic field parallel to the surface, does not decrease approaching the surface and penetrates through the hole to a depth equal to the diameter of the hole.²⁵ A thin conducting sheet immersed in a parallel magnetic field will displace the magnetic field to exclude it from the interior of the conductor, but the field at the surface of the conductor (and inside a hole with diameter large compared to the thickness of the sheet) will be nearly the same as the field before inserting the sheet. Therefore, inserting a thin metal gasket into a parallel MW magnetic field leaves the MW field nearly unchanged across the face of the gasket and at the end of the gasket hole where the NVND sensor is located. The MW field is delivered to the DAC using a microstrip transmission line etched on a double-sided printed circuit board (25 μm copper cladding on 1.55 mm thick epoxy-fiberglass core), shown in Figs. 1 and 2(a). The MW magnetic fields are driven by current flowing parallel to the transmission line axis (y) in the top conductor and anti-parallel return current in the ground plane, with the magnetic field looping around the narrow top conductor, as shown in Fig. 2(b). The DAC gasket and NVND sensor are placed between the top conductor and the ground plane of the microstrip, inside a 2 mm hole drilled through the microstrip, as shown in Fig. 2(b). The hole is drilled 1/4 wavelength (13 mm) from the open end of the transmission line [see Fig. 2(a)]. The MW field is reflected at the open end of the line, producing a standing wave with doubled magnetic field amplitude at the anti-node (hole). A circulator with 50 Ω terminator on its third port is inserted between the MW source and the microstrip, as shown in Fig. 2(c), so the reflected power does not go back to the MW source.

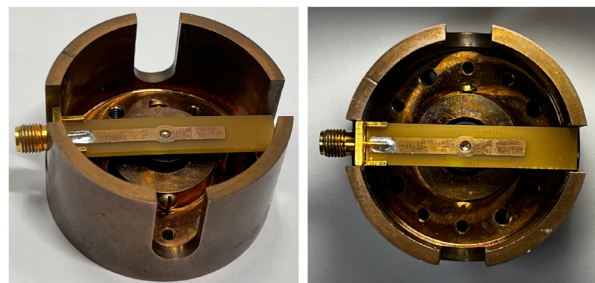


FIG. 1. Microstrip MW antenna attached to the DAC cylinder with a gasket in the microstrip hole (side and top view).

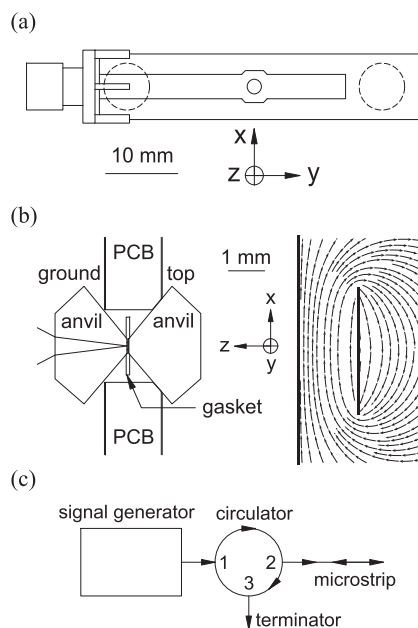


FIG. 2. (a) Microstrip MW antenna on the printed circuit board (PCB), with SMA coaxial connector soldered to the left end and with a 2 mm hole drilled 13 mm from the open circuit right end. The 3.4 mm wide top conductor gives nearly 50 Ω characteristic impedance for the transmission line. The top conductor is widened to 4.4 mm at the position of the hole. Threaded brass mounting posts of 6 mm diameter (dashed circles) are soldered to the ground plane on the PCB back side using a fixture to correctly position the posts with respect to the hole. (b) Cross section through the center of the DAC, showing the diamond anvils (2.0 mm thick, 400 μm culet) inserted into the 2 mm hole in the 1.6 mm thick microstrip PCB, with the 1.6 mm diameter gasket compressed between the diamond anvil culets. Light is collected (NA = 0.25) from the NVND layer deposited on the left culet, through the ground plane of the microstrip. The MW magnetic field distribution for the microstrip transmission line is shown on the right (same scale). MW propagation is along y and B_{MW} at the gasket is along x . (c) A Rigol DSG836 signal generator drives the microstrip.

The hole in the microstrip perturbs the MW magnetic field, which bulges out of the hole in the ground plane and the top conductor, but the field distribution at the position of the gasket and NVND sensor remains nearly uniform and parallel to the ground plane. The MW field of the microstrip was probed using ODMR in the NVND

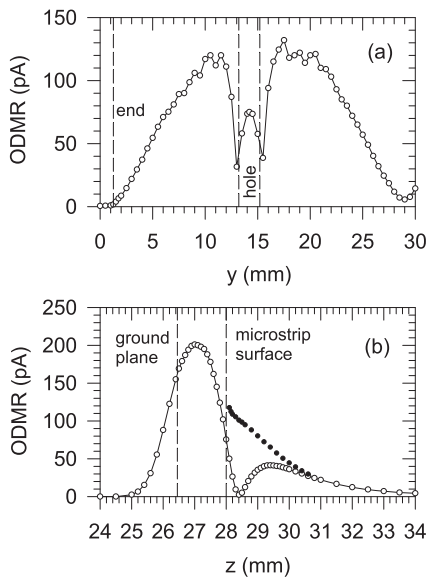


FIG. 3. Microstrip MW magnetic field intensity at 2882 MHz measured using ODMR fiber probe, with the MW field \propto ODMR signal. (a) Longitudinal scan at the top surface of the microstrip, starting from the open end, showing the standing wave anti-node at the hole position. (b) Vertical scan on the axis of the hole in the microstrip, showing the maximum between the conductors and the node just above the top surface where the field direction changes sign. The field above the microstrip without a hole is shown by the filled circles, obtained by a vertical scan taken 3 mm from the center of the hole.

coating on the end of a 105 μm multimode optical fiber, where the fiber transmits the excitation and fluorescence light to and from the NVND layer. The MW magnetic field node at the microstrip open end and the anti-node at the hole are seen in Fig. 3(a), where the MW field is measured as a function of the distance from the open end of the microstrip, with the NVND probe touching the top surface of the microstrip. The MW field on the axis of the hole, also measured with the fiber probe, is shown in Fig. 3(b). The MW magnetic field between the conductors is larger than the field outside, with the maximum 0.2 mm below center (closer to the ground plane) and a node 0.4 mm above the top conductor. The microstrip is mounted on the DAC with the NVND coated anvil placed at the maximum MW field position. The MW field between the conductors is a nearly transverse electromagnetic (TEM) wave propagating with velocity $v = c/\sqrt{\epsilon_r}$, where $\epsilon_r \approx 4$ is the effective relative permittivity of the 1.5 mm thick dielectric. MW power 100 mW traveling in the 50 Ω transmission line produces a 2.2 V potential difference between the conductors, with $E = vB \approx 1.5$ V/mm and $B \approx 0.10$ G, and produces a linear polarized standing wave MW field with amplitude $B_{MW} \approx 0.2$ G (circular polarized components $B_{\pm} = B_{MW}/\sqrt{2}$ and Rabi frequency = 2.8 MHz/G $\times B_{\pm} \approx 0.4$ MHz).

III. NV NANODIAMOND (NVND) DROP CASTING

Fluorescent diamond powders are commercially available with NV^- centers at a concentration up to 3.5 ppm (parts per million) in particles with sizes from 10 nm to 100 μm , so a deposited NVND sensor layer can be produced without the special facilities needed

to produce diamond anvils with implanted NV layers. NVND used in this work was obtained from Adamas Nanotechnologies. A sensor layer with uniform response across the layer is desired, but the ODMR signal varies with the orientation of a NV diamond particle. Uniform response is obtained using randomly oriented particles that are small and numerous enough that the signal from the particles in the beam spot is the average over all orientations. The particles should be smaller than 1 μm to give good orientation averaging for a 3.5 μm beam spot and a 1 μm layer. A 1 μm thick layer of 140 nm, 3 ppm NVND is translucent, forward scattering 80% of incident laser light at 532 nm, back scattering 20%, and absorbing 0.2%. The simplest deposition technique is drop casting, where a drop with the particles in suspension is placed on the surface to be coated and the solvent is evaporated to leave behind a layer of particles. The result is often an extremely uneven layer with all the particles deposited in a thin ring at the edge of the drop, known as the coffee ring effect.²⁶ Due to the practical importance of drop casting, this effect and its mitigation have received extensive investigation.^{26–31} Drop cast layers of 40–140 nm NVND particles deposited from water suspension show the coffee ring effect, with the largest effect for the smallest particles. One way to reduce the coffee ring effect is to increase the evaporation rate so that the drop surface descends faster than the particles can diffuse away, so the particles get trapped at the descending drop surface.²⁸ Another way is to use a surfactant that traps the particles at the drop surface by electrostatic interactions.³⁰ We have used both schemes. The NVND particles have a carboxyl surface functionalization, which gives them a negative surface charge to reduce particle aggregation. Adding a cationic surfactant (disinfectant containing octyl decyl dimethyl ammonium chloride and C_{14} alkyl dimethyl benzyl ammonium chloride) at 3 ppm concentration gives a positively charged surface to the drop, which will tend to trap the NVND particles at the drop surface. Surface trapping by fast evaporation is also enabled by raising the drop temperature to 80 $^{\circ}\text{C}$.

The thickness of a layer and its uniformity can be assessed from fluorescence intensity as an excitation spot is scanned across the deposit. Average thickness is determined from the mass of deposited NVND diamond and the area of the deposit. The average fluorescence intensity determined from the integral of the fluorescence measured in a scan along the diameter of the deposit, assuming circular symmetry and fluorescence proportional to thickness, calibrates the thickness/fluorescence ratio. Figure 4(a) shows a layer deposited at 80 $^{\circ}\text{C}$ onto Cu without surfactant, where the coffee ring effect is reduced but not eliminated, and Fig. 4(b) shows a more uniform layer deposited at 80 $^{\circ}\text{C}$ with surfactant. For the typical deposition in Fig. 4(b), the 1 mg/ml suspension of 140 nm NVND in water was sonicated to break up aggregates, and then, 30 μl of NVND suspension was mixed with 10 μl of 16 ppm by weight cationic surfactant solution. Drop cast layers are made using 5 μl drops of this suspension, which produce a 3.1 mm diameter spot on the substrate surface. Each drop is evaporated to dryness, and then, another is deposited on the same spot. Eight drops deposited on the same spot give a layer with 1.2 μm average thickness. Surfactant can be removed from the deposit by gently rinsing with acetone. The surfaces to be coated are usually much smaller than the 3 mm drop diameter. To coat the culet of a diamond anvil, a thin brass mask is prepared using electric discharge machining to make a conical hole with opening matching the culet diameter and taper matching the

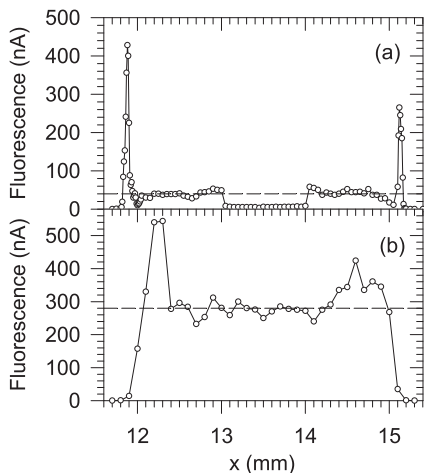


FIG. 4. The thickness of layers of 140 nm NVND is measured by fluorescence in scans across spots deposited at 80 °C. (a) Without surfactant, the deposit from a single 5 μl drop has a tall coffee ring 40 μm wide, around a 140 nm thick NVND monolayer (dashed line), around a 1 mm diameter bare center. (b) With surfactant, a more uniform layer 1.0 μm thick (dashed line) is deposited from eight successive 5 μl drops. The scanning spot diameter is (a) 6 μm or (b) 300 μm .

pavilion slope. The mask is clamped over the diamond anvil with the culet filling the opening, culet surface level with the mask surface. After the NVND layer is deposited on the mask and culet, the mask is removed and the excess NVND layer on the culet is scraped off to leave a sensor patch of the desired size. In a similar fashion, the cleaved end of the 105 μm multimode optical fiber used to probe the microstrip MW field was coated using a matching SMA fiber ferrule slipped over the fiber as the mask, with the fiber end level with the ferrule surface.

IV. OPTICAL DETECTED MICROWAVE RESONANCE (ODMR) APPARATUS

The optical apparatus for continuous wave optical detected magnetic resonance is shown in Fig. 5. Light at 532 nm delivered

on an optical fiber is collimated and directed toward the DAC by using a dichroic beam splitter. A lens focuses the 532 nm light onto the NVND layer in the DAC, and the fluorescent light from the NVND layer is collected and collimated by the same lens. The beam of red fluorescent light passes through the dichroic beam splitter and another spectral filter to a second beam splitter, which sends 70% of the light to the photodiode detector. The remainder of the light is focused by a long focal length lens to form a magnified image of the DAC sample space on the camera sensor. The light source is a laser, and the beam is attenuated and then coupled into a single mode optical fiber with 3.5 μm mode field diameter. The excitation power delivered to the DAC is in the range from 1 μW to 30 mW. The collimating and focusing lenses are both molded glass aspheric lenses with 11 mm focal length, which image the fiber end to form a 3.5 μm excitation spot on the NVND layer. The numerical aperture (NA) of the lens for fluorescent light collection is 0.25. The aspheric lenses are not achromatic, so a lens with -1000 mm focal length is inserted between the collimating lens and the dichroic beam splitter to compensate for the difference in focal length for the focusing lens at 532 and 700 nm. The aspheric focusing lens is mounted on the DAC with the NVND layer at its focus, and the orientation of this unit is adjusted to center the image of the DAC sample space on the camera sensor. The camera image shows the position of the excitation spot (fluorescent spot) inside the DAC, and the pointing of the fiber collimator controls the position of the excitation spot on the sample. The apparatus can be configured for confocal detection by fiber coupling the fluorescent light to the photodiode using another fiber collimator placed at the PD position in Fig. 5 so that light is collected from a sample spot with position and size determined by the pointing of this fiber collimator and the fiber diameter. The apparatus can also be used with light coupled to an optical fiber probe placed at the DAC position in Fig. 5. The non-magnetic piston-cylinder (modified BX90) DAC is made of a copper-beryllium alloy (Cu-Be) using cubic boron nitride (CBN) seats, a MP35N alloy (35 Ni, 35 Co, 25 Cr, 10 Mo) gasket, and brass screws, except for the four titanium screws that compress the DAC. The thermal expansion of the Cu-Be shell and titanium screw combination very nearly matches the thermal expansion of the Cu-Be, CBN, and diamond stack that is being compressed by the screws (differential thermal expansion coefficient $1.5 \times 10^{-7}/\text{K}$), so changing the DAC temperature causes little change

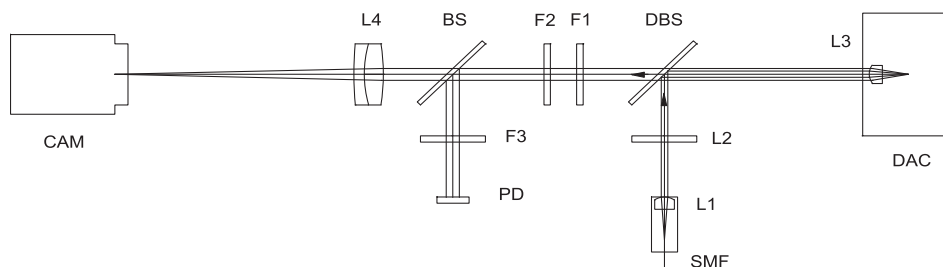


FIG. 5. Optics for ODMR measurements. Excitation light at 532 nm is delivered by the single mode optical fiber SMF (460HP, NA = 0.13), collimated by aspheric lens L1 ($f = 11$ mm), reflected by the dichroic beam splitter (DBS) (transmit $\lambda > 567$ nm), and focused by aspheric lens L3 ($f = 11$ mm) onto the NVND sensor layer in the diamond anvil cell (DAC). The fluorescent light at about 700 nm from the NVND layer is collected and collimated by the same lens L3 (NA = 0.25). Lens L2 ($f = -1000$ mm) compensates for the chromatic aberration of L3. The fluorescent light beam passing through filters F1 ($\lambda > 550$ nm) and F2 ($\lambda > 570$ nm) is divided by the beam splitter (BS), with 70% going through filter F3 ($\lambda < 800$ nm) to the PIN photodiode PD and with the remainder focused by achromatic lens L4 ($f = 100$ mm) to form a magnified image of the DAC sample chamber on the sensor of the camera CAM.

in pressure. The DAC is enclosed in a mu-metal magnetic shield can, with axial optical access ports and side cutouts for the microstrip entry. Thermal expansion compensation and an attached aspheric lens facilitate the use of the DAC inside a cryostat. A signal generator (Rigol DSG836) delivers up to 100 mW MW power to the DAC using the microstrip shown in Figs. 1 and 2. Magnetic resonance is detected by the reduction in the fluorescence by about 1% when the MW frequency is tuned to resonance. The MW excitation is amplitude modulated sinusoidally at 200 Hz, and the photodiode current is sent to a lock-in detector (Stanford Research Systems SR810) measuring the rms (root-mean-square) photodiode current amplitude at the modulation frequency. The lock-in output recorded on a digital oscilloscope (Tektronix TDS 2022C) during the sweep of the MW frequency is the ODMR spectrum. Typical NVND ODMR spectra are shown in Fig. 6(a) for several applied magnetic fields. Increasing the magnetic field broadens the spectrum and reduces the peak ODMR signal. Contrast between the ODMR signal and background

fluorescence is given by the ratio of the rms current amplitude measured by the lock-in and the average photodiode current ($[\text{maximum} - \text{minimum}]/\text{average current}$ is $2\sqrt{2} \approx 2.8\times$ larger). Contrast is 0.63% at the peak of the $B = 0$ G spectrum in Fig. 6(a), 0.70% in Fig. 10(b), and 0.60% in Fig. 11(a). The current noise is 0.3 pA rms, with about equal contributions from shot noise and 0.13 pA/ $\sqrt{\text{Hz}}$ lock-in amplifier input noise in the 2.6 Hz bandwidth. The magnetic field sensitivity is 0.02 G/ $\sqrt{\text{Hz}}$ ($=2 \mu\text{T}/\sqrt{\text{Hz}}$) based on the current noise and the ODMR signal slope at the steep edge of the 30 G spectra in Figs. 6(a) and 10(a). The magnetic field magnitude is simply determined from the measured width $\Delta\nu_B$ of the spectrum, with the zero field width $\Delta\nu_{B=0}$ subtracted, using the following expression:

$$B_W = (\Delta\nu_B^2 - \Delta\nu_{B=0}^2)^{1/2} / (2g_e\mu_B), \quad (1)$$

where $g_e\mu_B = 2.80$ MHz/G. The width $\Delta\nu_B$ is the full width at half maximum (FWHM). Since the spectrum is double-peaked, the half-height point on the left (right) is determined using the height of the left (right) peak. Equation (1) was used to determine the magnetic field from the spectra in Fig. 6(a), for applied fields in the range $1 < B < 40$ G directed perpendicular to the MW magnetic field, with results shown in Fig. 6(b). The error in the field determined using Eq. (1) was ± 0.1 G for $1 \leq B \leq 5$ G and $\pm 1\%$ for $5 \leq B \leq 40$ G. The minimum field that can be measured is limited by the width of the zero field spectrum. An advantage of NVND ensemble magnetometry is insensitivity to the magnetic field direction. Since the number of NV aligned with the applied field in the NVND layer is independent of the applied field direction, the maximum splitting measures the magnitude of the applied magnetic field. However, the FWHM of the spectrum is reduced and the magnetic field is underestimated using Eq. (1) when the applied field is parallel to the MW field. The error is 18% when the angle between the applied and MW fields is 0° , 5% when the angle is 30° , and $<1\%$ when the angle is $>60^\circ$ (Fig. 10 of the Appendix). The average error for random field directions is 2%.

V. NV NANODIAMONDS (NVNDs) UNDER PRESSURE IN A DIAMOND ANVIL CELL

A DAC with a NVND sensor layer was used to observe the NVND ODMR spectrum under pressure. The DAC is prepared with the microstrip removed since it is difficult to work inside the 2 mm hole in the microstrip. The gasket for the 400 μm diameter diamond anvils is formed from a MP35N disk 1.6 mm diameter and 120 μm thick, indented, and laser drilled. After forming the gasket, the culet of the cylinder diamond anvil is coated with a 140 nm (3 ppm NV^-) NVND layer 0.5, 1, or 2 μm thick, and the excess is removed to leave the NVND sensor patch. The gasket is replaced, and the DAC is closed so that the gasket can be glued to one of the diamond anvils. With the gasket attached to the anvil, the DAC is opened again, a ruby pressure sensor is added, the microstrip is put in place, and the DAC is closed. For this experiment, the gasket was initially 34 μm thick with a 300 μm hole, the NVND sensor patch was 150 μm wide, and the DAC was filled with He gas at 3 kbar as the pressure transmitting medium (PTM). Figure 7 shows experimental results for 0.5, 1, and 2 μm thick NVND layers in a DAC with He PTM at 20 $^\circ\text{C}$, at pressures measured using ruby fluorescence.^{32,33} He was used as the PTM to ensure nearly hydrostatic conditions in the DAC. He solidifies at 11.8 GPa at 298 K, but the stress remains

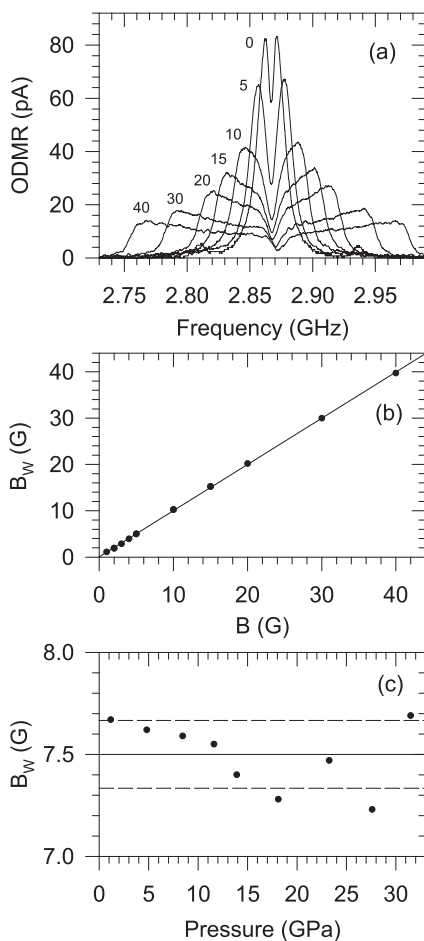


FIG. 6. (a) Ambient pressure (1 bar, 20 $^\circ\text{C}$) ODMR spectra for NVND with the applied magnetic field direction perpendicular to the MW magnetic field of the microstrip, measured for several field magnitudes from 0 to 40 G. Magnetic field B_W is determined from the width of the ODMR spectrum using Eq. (1) at (b) ambient pressure and (c) at high pressure inside the DAC.

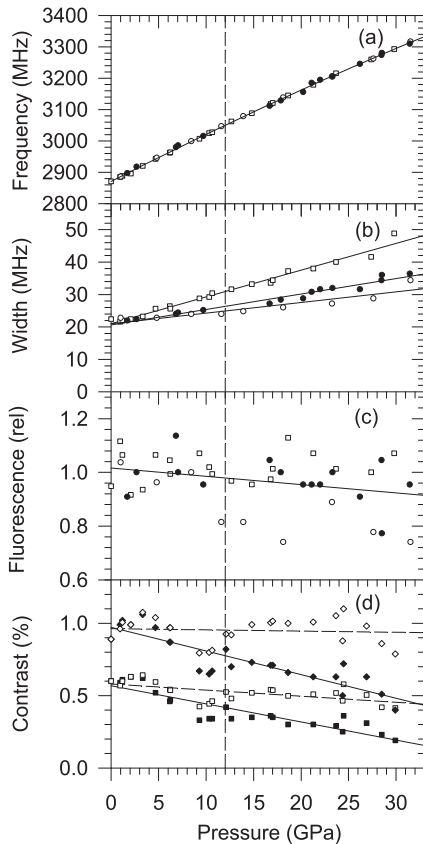


FIG. 7. Measured ODMR (a) center frequency, (b) stress broadening (FWHM), and (c) fluorescence intensity/intensity($P = 0$) for NVND layers of thicknesses $0.5 \mu\text{m}$ (open circles), $1 \mu\text{m}$ (filled circles), or $2 \mu\text{m}$ (open squares) in a DAC with He PTM, $B = 0$ G and 2 mW laser power on a $5 \mu\text{m}$ diameter spot. (d) Peak contrast measured for the $2 \mu\text{m}$ NVND layer with 2 mW laser power on a spot with $5 \mu\text{m}$ diameter (square symbols and bottom curves) or $50 \mu\text{m}$ diameter (diamond symbols and top curves), showing lower contrast at higher laser intensity. ODMR spectral broadening accounts for decreasing contrast with increasing pressure, as shown by the open symbols and dashed curves where contrast has been multiplied by width/width ($P = 0$). The vertical dashed line marks the He solidification pressure. The curve fit to the data in (a) is $\nu_D = a + bP + cP^2$ with $a = 2871(1)$ MHz, $b = 15.5(2)$ MHz/GPa, and $c = -0.044(7)$ MHz/GPa².

quasi-hydrostatic above 11.8 GPa,³⁴ so only small broadening of the ODMR peak was expected due to PTM uniaxial stress above 12 GPa (see the Appendix). Contrary to expectations, Fig. 7(b) shows that the ODMR spectrum of the NVND layer broadens steadily starting at 0 GPa, there is no inflection at the He solidification pressure, and the broadening at 30 GPa is much larger than the expected 0.7 MHz broadening due to uniaxial stress in the He PTM. The width of the ODMR spectrum measured for the $2 \mu\text{m}$ NVND layer increases from 23 MHz (FWHM) at ambient pressure to 49 MHz at 30 GPa. The ODMR spectral width for 0.5 and $1 \mu\text{m}$ NVND layers also increases steadily but more slowly with pressure, reaching 32 and 36 MHz at 32 GPa. This broadening is accounted for by random stress in jammed particles in the NVND layer compressed by the PTM (see

the Appendix). The ODMR peak frequency ν_D as a function of pressure P is not affected by the additional random stress S in the NVND layer (see the Appendix), so the present results for $\nu_D(P)$ in Fig. 7(a) should agree with previous work. The present results can be compared with recent ODMR measurements for $\nu_D(P)$ at pressures up to 140 GPa.⁷ The fit of $\nu_D = a + bP + cP^2$ to those measurements gave $b = 14.8(1)$ MHz/GPa and $c = -0.027(7)$ MHz/GPa²,⁷ as compared to $b = 15.5(2)$ MHz/GPa and $c = -0.044(7)$ MHz/GPa² for the fit to data up to 32 GPa in Fig. 7(a). The curvature coefficients c disagree, but c determined using the fit with the much larger range for P may be more reliable. Repeating the fit to the data in Fig. 7(a) using $c = -0.027$ MHz/GPa² as a constraint gives $b = 14.9(1)$ MHz/GPa, now in agreement with the result of the previous work. Several other experiments have determined b by fitting a linear function $\nu_D = a + bP$ to the measurements, with results $b = 14.6(1)$ for $P < 60$ GPa,¹² $11.7(7)$ for $P < 8$ GPa,¹³ $14.9(2)$ for $P < 6$ GPa,¹⁴ and $14.9(5)$ for $P < 40$ GPa.¹⁹ High fluorescence intensity and ODMR contrast enable more sensitive measurements. Recent measurements for $1 \mu\text{m}$ NV microdiamonds in a DAC found fluorescence intensity decreasing by 90% over the 0–30 GPa range [Fig. 2(c) of Ref. 7]. This disagrees with the present results in Fig. 7(c) that show the NVND fluorescence intensity is nearly constant with increasing pressure over this range. Figure 7(d) shows decreasing contrast with increasing pressure, but the contrast decrease is accounted for by the spectral broadening. The magnetic field in the DAC is simply determined from measurements of the width of the spectrum using Eq. (1). Strain, electric, and magnetic field broadening contributions add approximately in quadrature, so the magnetic field can be accurately determined when the magnetic field broadening contribution is not small compared to the other contributions. A small permanent magnet was used to apply a field $B = 7.5$ G ($2g_e\mu_B B = 42$ MHz) to the $0.5 \mu\text{m}$ NVND layer in the DAC, and the B values were determined from the ODMR spectrum using Eq. (1) at nine pressures from 1 to 32 GPa. The measured B field values, shown in Fig. 6(b), are randomly distributed around the average with 2% standard deviation, consistent with the reproducibility of the applied field.

VI. MAGNETIC FIELD OF IRON SPHERE

A DAC with a NVND sensor layer was used to observe the ferromagnetic transition in iron under pressure, with B determined using Eq. (1) from ODMR spectra similar to those in Fig. 6(a). Results are shown in Fig. 8. The sample is an iron sphere produced by an electric spark between two thin (thermocouple grade) iron wires under argon gas in a glove box (<0.5 ppm O_2 and H_2O to avoid oxidation, verified by Raman spectroscopy^{35,36}). The molten iron drops that are produced freeze in flight and are collected on a glass slide 5 cm below. Sparks in air produce oxidized iron spheres around which a 20 G magnetic field is measured at pressures up to 36 GPa. The DAC is prepared as in Sec. V, with the microstrip removed. The MP35N gasket for the $400 \mu\text{m}$ diameter diamond anvils is $44 \mu\text{m}$ thick with a $300 \mu\text{m}$ hole. The $1 \mu\text{m}$ thick 140 nm NVND sensor layer is deposited and trimmed to a $140 \times 100 \mu\text{m}^2$ patch, and then, the gasket is glued to the cylinder diamond anvil with the NVND sensor. The $11.4 \mu\text{m}$ diameter iron sphere sample and a ruby ball pressure sensor are placed on the facing piston diamond anvil, the microstrip is installed, and the DAC is closed and filled with 3 kbar He gas as the PTM. Due to the high

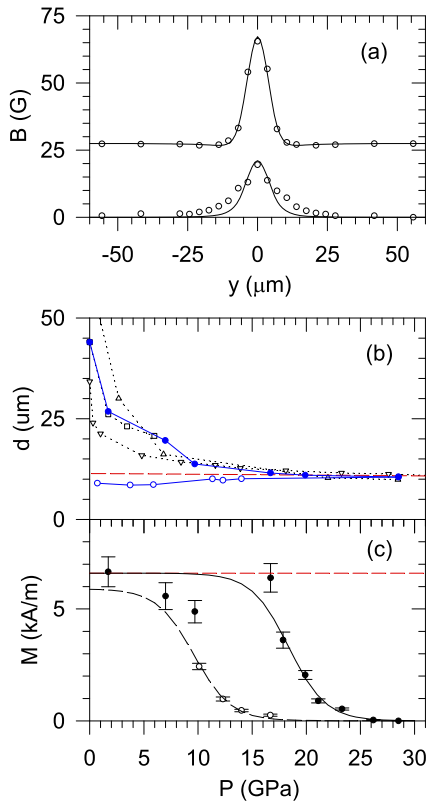


FIG. 8. (a) Scans of the magnetic field along a line below the center of an 11.4 μm iron sphere at 16.7 GPa with applied field $B_0 = 27.5$ G (top data and curve) and $B_0 = 0$ G (bottom data and curve). (b) Pressure dependence of the distance d between the diamond culets for gaskets with initial thicknesses 34, 44, and 61 μm and hole diameter 300 μm . The results in (a) and (c) were obtained in the DAC run shown by the blue solid curve and circles. The red dashed line shows the diameter of the iron sphere. (c) Magnetization of the iron sphere with the 27.5 G applied external field as a function of increasing pressure (solid circles and curve) and decreasing pressure (dashed curve). The horizontal red dashed line is magnetization induced in a sphere with permeability $\mu/\mu_0 \gg 1$.

compressibility of the He PTM (5.7 times volume decrease as pressure increases from 0.3 to 30 GPa)^{37,38} the gasket thickness decreases to 1/2 initial thickness at 3 GPa and 1/4 initial thickness at 30 GPa, and the gasket hole contracts to 230 μm mean diameter.³⁹ The final gasket thickness is slightly smaller than the iron sphere diameter, although the plan was for the gasket thickness to remain larger than the sphere diameter. As shown in Fig. 8(b), the same final gasket thickness is obtained starting with 34, 44, or 61 μm initial gasket thickness, while the contracted gasket hole becomes more elliptical as the initial thickness increases. The gasket thickness further decreases as the pressure is decreased from the maximum. Pressure decrease for the fluid He PTM is accomplished by reducing the closing force on the DAC to leak PTM and then increasing the force to reseal the DAC, incrementally thinning the gasket. At each pressure, the iron sample in the DAC was magnetized to saturation by applying $B_0 = 5$ kG parallel to the DAC axis (z). Then, the field of the iron sphere was measured from ODMR spectra similar to those in Fig. 6(a), first with external field $B_0 = 0$ G and then with external

field $B_0 = 27.5$ G. Measurements were made along a line parallel to the microstrip axis (y) in a plane parallel to the DAC axis (z) passing through the center of the sphere so that the measured magnetic field vector B is perpendicular to B_{MW} (x) by symmetry. The center of the iron sphere is a distance h above the NVND sensor layer, so taking the origin of coordinates as the sphere center, the field B is measured at positions (y, h) . At each pressure, h was determined using the sphere diameter and the gasket thickness obtained from a measurement of the optical path difference between the diamond anvils divided by the He refractive index.⁴⁰ The sphere diameter contraction (0.7 μm at 30 GPa) is calculated using the equation of state for iron.^{41,42}

For a sphere of radius R with uniform magnetization M along z and zero external field, the magnitude of the field at NVND sensor position (y, h) is

$$B = (\mu_0 MR^3/3)[(2h^2 + y^2)^2 + h^2 y^2]^{1/2}/(h^2 + y^2)^{5/2}, \quad (2)$$

while the field magnitude B with external field B_0 applied along z is

$$B = \left([(\mu_0 MR^3/3)(3hy)/(h^2 + y^2)^{5/2}]^2 + [B_0 + (\mu_0 MR^3/3)(2h^2 - y^2)/(h^2 + y^2)^{5/2}]^2 \right)^{1/2}. \quad (3)$$

Directly below the sphere center, at $y = 0$, the last expression reduces to

$$B = B_0 + (2/3)(R/h)^3 \mu_0 M. \quad (4)$$

The magnetization of a linear permeable sphere in external field B_0 is

$$\mu_0 M = 3B_0(\mu - \mu_0)/(\mu + 2\mu_0), \quad (5)$$

with limit

$$\mu_0 M_{\text{max}} = 3B_0 \quad (6)$$

for $\mu \gg \mu_0$. Figure 8(a) shows the magnetic field of the 11.4 μm diameter iron sphere measured by the NVND sensor layer in the DAC at 16.7 GPa. Confocal detection from a 30 μm spot centered on the excitation spot was used to eliminate the diffuse fluorescence produced by laser light reflected from the iron sphere onto the NVND layer. The magnetic field was determined from the width of the ODMR spectrum using Eq. (1) at each position along the line $h = 5.8$ μm below the center of the iron sphere. The zero field width $\Delta\nu_{B=0}$ is measured far from the magnetized sphere with applied field $B_0 = 0$. Equation (3) convolved with the Gaussian function for the 3.5 μm diameter laser beam spot was fit to the $B_0 = 27.5$ G data points. A good fit is obtained, and the magnetization $M = 6.4 \pm 0.6$ kA/m (1 kA/m = 1 emu/cm³) determined from the fit is close to the value $M_{\text{max}} = 6.6$ kA/m predicted by Eq. (6). Equation (2) convolved with the Gaussian for the laser spot was fit to the $B_0 = 0$ G data points, but this function does not fit the broad wings of the observed peak. The remnant magnetization determined from this fit is $M = 2.9 \pm 0.3$ kA/m, which is 0.17% of the saturation magnetization $M_s = 1713$ kA/m for iron at ambient pressure and temperature.⁴³

Magnetic field scans similar to those in Fig. 8(a) were made at increasing and then decreasing pressures. At the initial low pressure,

the sphere starts far above the NVND layer and the B field is reduced by the factor $(h/R)^{-3} = 1/51$, but this factor increases until it reaches 1 when the sphere touches the NVND layer at 18 GPa [see Fig. 8(b)]. The remnant field is too small for reliable measurements until the sphere is nearly in contact with the NVND layer, but with an external magnetic field applied, the magnetization of the sphere is well determined at all separations. The magnetization M measured with $B_0 = 27.5$ G applied is plotted vs P in Fig. 8(c), which shows M vanishing at high pressure. The magnetic transition pressure was determined from a fit of the function

$$M = M_{\max}/[1 + \exp((P - P_0)/\Delta P)] \quad (7)$$

to the $M(P)$ data, where $M_{\max} = 6.6$ kA/m for an iron sphere in the applied field is obtained using Eq. (6). The fit to the increasing pressure data in Fig. 8(c) gives $P_0 = 18.4 \pm 0.5$ GPa and $\Delta P = 1.7 \pm 0.2$ GPa for the position and width of the ferromagnetic transition. Remnant field measurements exhibit the same transition but are less accurate. Previous ODMR measurements of this transition find magnetization falling to half at 16 GPa¹⁶ or 20 GPa.¹⁸ The magnetization was also determined for decreasing pressures, as the iron sphere was progressively deformed into an $11.8 \times 9.8 \mu\text{m}^2$ elliptical cylinder $8.5 \mu\text{m}$ high at 0.7 GPa. Figure 9 shows the DAC sample chamber at the end of this experiment. For pressures down to 10 GPa, the sample was approximated as an oblate spheroid, where the axial/equatorial ratio reached 0.87 with demagnetization factor 0.37^{44,45} and $M_{\max} = 5.9$ kA/m at 10 GPa. Measurements below this pressure were rejected because of shape uncertainty and because the deforming sphere had pushed aside the NVND layer leaving a bare spot on axis, so a centered excitation spot measures only the smaller off-center field around the bare center. The fit of Eq. (7) to the decreasing pressure magnetization measurements in Fig. 8(c) with $M_{\max} = 5.9$ kA/m and $\Delta P = 1.7$ GPa gives $P_0 = 9.6 \pm 0.2$ GPa for the transition pressure. Previous ODMR measurements find 10 GPa¹⁶ and 14 GPa¹⁸ for this transition. The difference between the transition pressures for increasing and decreasing pressure is 8 GPa, as compared to 6 GPa from the previous ODMR measurements.^{16,18} The delayed back transformation with decreasing pressure in the present work may be related to the deformation of the iron sample in contact with the diamond anvils. Quantitative magnetic measurements are obtained for iron using the NVND sensor in a DAC at high pressure. The external applied field $B_0 = 27.5$ G produces magnetic

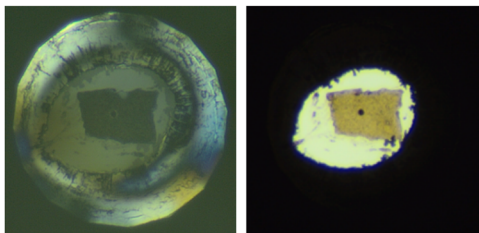


FIG. 9. Reflection (left) and transmission (right) microscope images of the DAC sample space following the experiment in Fig. 8(c), where the pressure was increased to 28.5 GPa and then decreased to 0.7 GPa. The iron sample is the dark dot on the rectangular $140 \times 100 \mu\text{m}^2$ NVND sensor patch, near the center of the $400 \mu\text{m}$ culet. Fragments of the $15 \mu\text{m}$ ruby ball are at the lower right corner of the NVND patch, near the edge of the $260 \times 200 \mu\text{m}^2$ gasket hole.

broadening, which dominates all other contributions to the ODMR peak width, so the broadening is linear in B and the ODMR width measures the magnetic field averaged over the excitation spot. Stress broadening of the zero field ODMR spectrum to 36 MHz at 29 GPa has negligible effect on the accuracy of the magnetic field determination. The good fit of Eq. (3) to the measurements in Fig. 8(a) indicates that the assumed dipole field for a uniformly magnetized sphere is a good approximation even at the surface to the sphere.

VII. CONCLUSION

This work describes apparatus and techniques for magnetometry in a DAC, including a microstrip MW antenna design compatible with simple metal gaskets, and procedures for preparing the NVND sensor for the DAC. The contributions to the ODMR spectrum for the NVND sensor are analyzed, and it is shown that the magnetic field magnitude can be simply and accurately determined from the width of the ODMR spectrum. Excess broadening of the NVND sensor ODMR spectrum is observed and investigated at pressures up to 30 GPa. Magnetometry in a DAC using the NVND sensor is demonstrated by measurement of the ferromagnetic transition in iron at 18 GPa. Magnetic measurements for the small sample in a DAC have been difficult and infrequent. This has not changed even after several demonstrations of ODMR magnetometry in a DAC. The present work describes a simple NV ODMR magnetometry platform for DAC work, which can make NV magnetometry in a DAC more widely accessible.

ACKNOWLEDGMENTS

We thank Paul B. Ellison who designed and constructed the DAC. This work was supported by the U.S. Department of Energy, Office of Basic Energy Sciences, under Award No. DE-SC0020303 and, in part, by the Gordon and Betty Moore Foundation's EPiQS Initiative, Grant No. GBMF10731.

AUTHOR DECLARATIONS

Conflict of Interest

The authors have no conflicts to disclose.

Author Contributions

David P. Shelton: Conceptualization (lead); Data curation (equal); Formal analysis (lead); Investigation (equal); Writing – original draft (lead); Writing – review & editing (lead). **Waldo Cabriales:** Data curation (equal); Investigation (equal); Writing – review & editing (supporting). **Ashkan Salamat:** Conceptualization (equal); Funding acquisition (lead); Investigation (equal); Writing – review & editing (supporting).

DATA AVAILABILITY

The data that support the findings of this study are available from the corresponding author upon reasonable request.

APPENDIX: OPTICAL DETECTED MICROWAVE RESONANCE (ODMR) SPECTRUM

The magnetic resonance spectrum for a single NV center is a pair of peaks, where the splitting is mainly due to the magnetic field along the NV axis and the electric field and strain perpendicular to the NV axis. The spectrum for an ensemble of NV centers is the sum of all the different spectra from the individual NV centers. ODMR spectra measured for several values of the magnetic field magnitude and direction are shown in Figs. 6(a) and 10. The spectra were obtained using the NVND coated optical fiber probe placed on the surface of a microstrip, in the magnetic field from a solenoid or Helmholtz coils. The NV⁻ concentration in the 70 nm NVND coating is 3.5 ppm. The spectra are similar to those previously observed for NVND ensembles.⁴⁶ The spectrum with zero applied magnetic field at ambient pressure is a peak with a sharp central dip and broad tails. This spectrum results from electric field splitting due to nearby charged defects, including other NV⁻ centers in the NVND.^{8,9} The distribution of electric field magnitudes that was determined by a

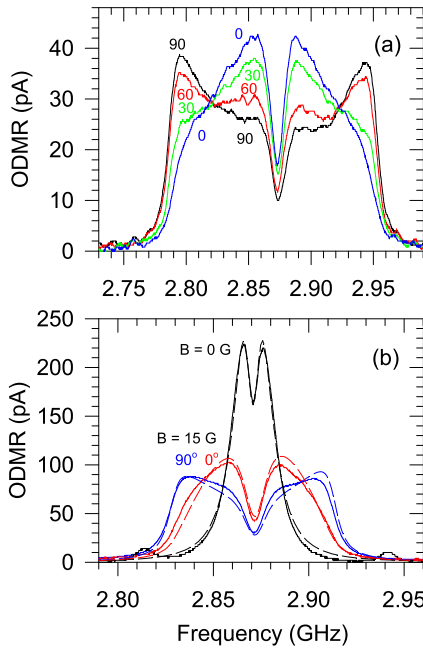


FIG. 10. (a) Ambient pressure (1 bar, 20 °C) ODMR spectra measured for NVND with the 30.0 G applied magnetic field in the plane of the microstrip, for several angles from 0° to 90° between the applied and MW field directions. FWHM is 169.8, 168.6, 160.6, 141.6 MHz for 90°, 60°, 30°, 0°, respectively. The zero field width is 25.6 MHz, and the fields B_W determined using Eq. (1) at the corresponding angles are 30.0, 29.8, 28.3, 24.9 G. (b) Comparison of experimental ODMR spectra (solid curves) and calculated spectra (dashed curves), for 0° and 90° angles between the applied and MW field directions. The calculated zero field spectrum is a fit of Eq. (A11) to the experimental data. The curves for $B = 15.0$ G are calculated from Eq. (A6) for 0° or Eq. (A11) for 90°, using $v_B = 42$ MHz and the zero field fit parameter values from the fit to the $B = 0$ G spectrum. The field B_W determined from the measured FWHM using Eq. (1) is 15.0 G at 90° and 12.3 G at 0°. The small satellite peaks in the experimental zero field spectrum at -57 and +70 MHz shift are due to NV⁻ centers with a ¹³C nearest-neighbor.⁵²

simulation with randomly distributed charged defects is fit by the following expression:⁸

$$f_E(\xi) = 2\pi \xi^{-5/2} \exp[-(4\pi/3)\xi^{-3/2}], \quad (\text{A1})$$

where $\xi = E/E_0$ is the scaled electric field magnitude. The component of the electric field perpendicular to the NV axis produces splitting χv_E , where $\chi = \xi \sin \theta_E$ is the scaled perpendicular field, θ_E is the angle between the electric field vector and the NV axis, and the perpendicular field distribution is

$$f_{Ep}(\chi) = \int_0^{\pi/2} d\theta_E f_E(\chi/\sin \theta_E) \approx 9590 \chi^{-9/2} \exp[-(10\pi/3)\chi^{-1/2}]. \quad (\text{A2})$$

The inhomogeneous broadening due to the different fixed splitting at each site is convolved with the homogeneous broadening by fluctuating fields to produce the observed profile.^{10,47,48} A magnetic field B parallel to the NV axis produces a Zeeman shift $v_B = \pm g_e \mu_B B$ and a splitting of the NV resonance, while a perpendicular field produces a shift $\propto B^2$. The magnetic field splitting adds in quadrature to the electric field splitting. The magnetic field of the nuclear spin on the ¹⁴N atom of the NV center, which has projection along the NV axis proportional to the quantum number $m_I = 0, \pm 1$, adds to any external applied magnetic field and further splits each peak into a triplet. Hydrostatic pressure in a DAC introduces a shift without broadening or splitting the ODMR peak, but when the fluid pressure transmitting medium (PTM) freezes under pressure,⁴⁹ the stress in the PTM becomes uniaxial.³⁴ The simplest uniaxial stress tensor σ_{ij} is axially symmetric and diagonal in the lab frame and is specified by the pressure $P = (\sigma_{xx} + \sigma_{yy} + \sigma_{zz})/3$ and the excess axial (axial-radial) stress $S = \sigma_{zz} - (\sigma_{xx} + \sigma_{yy})/2$. A rotation transforms this stress tensor to the NV frame oriented at θ, ϕ, ψ , where ψ is the rotation angle around the NV axis. In terms of the stress susceptibilities (MHz/GPa) $\alpha_1 = 8.6, \beta_1 = -2.5, \alpha_2 = -1.95, \beta_2 = -4.5$ ¹⁶ and the stress tensor components in the NV frame, the stress induced ODMR shift is^{7,16,50,51}

$$D^S = \alpha_1(\sigma_{xx} + \sigma_{yy}) + \beta_1 \sigma_{zz} = (2\alpha_1 + \beta_1)(P - S/3) + (\alpha_1 \sin^2 \theta + \beta_1 \cos^2 \theta)S, \quad (\text{A3})$$

and the two splitting contributions due to stress induced C_{3v} symmetry breaking are

$$E_x^S = \alpha_2(\sigma_{yy} - \sigma_{xx}) + 2\beta_2 \sigma_{xz} = (\alpha_2 \sin^2 \theta \cos 2\psi + \beta_2 \sin 2\theta \sin \psi)S \quad (\text{A4})$$

and

$$E_y^S = 2\alpha_2 \sigma_{xy} + 2\beta_2 \sigma_{yz} = (\alpha_2 \sin^2 \theta \sin 2\psi + \beta_2 \sin 2\theta \cos \psi)S. \quad (\text{A5})$$

The ODMR spectrum for an ensemble of randomly oriented NVND is given by

$$S(\nu) = A \int_0^\infty d\chi \int_0^\pi \sin \theta d\theta \int_0^{2\pi} d\phi \int_0^{\pi/2} d\psi \times f_L(\nu, \chi, \theta, \phi, \psi) f_{Ep}(\chi) [1 - (\sin \theta \cos \phi)]^2, \quad (\text{A6})$$

where

$$f_L = \sum_{m=-1}^1 \{ [1 + (v - v_D - \Delta v_D + v_{EBSm})^2 / v_L^2]^{-1} + [1 + (v - v_D - \Delta v_D - v_{EBSm})^2 / v_L^2]^{-1} \} \quad (\text{A7})$$

is the sum of six Lorentzian peaks with homogeneous width v_L , at positions determined by the electric, magnetic, and stress fields. The factor $f_{Ep}(\chi)$ accounts for the inhomogeneous distribution of site electric fields, and the factor $[1 - (\sin \theta \cos \phi)]^2$ accounts for the MW field projection, where the ODMR signal that is measured is proportional to the square of the MW field component perpendicular to the NV axis. The applied magnetic field and stress shift the center of the spectrum from the zero field frequency v_D by the amount

$$\Delta v_D(\theta, \phi) = (3/2)v_B^2(1 - n_B^2)/v_D + (2\alpha_1 + \beta_1)(P - S/3) + (\alpha_1 \sin^2 \theta + \beta_1 \cos^2 \theta)S \quad (\text{A8})$$

and produce a splitting given by

$$v_{EBSm}(\chi, m, \theta, \phi, \psi) = [(v_E \chi)^2 + (v_B n_B + v_I m)^2 + S^2(\alpha_2 \sin^2 \theta \cos 2\psi + \beta_2 \sin 2\theta \sin \psi)^2 + S^2(\alpha_2 \sin^2 \theta \sin 2\psi + \beta_2 \sin 2\theta \cos \psi)^2]^{1/2}. \quad (\text{A9})$$

Shift and splitting both depend on the projection of the applied magnetic field unit vector onto the NV axis, which is given by

$$n_B(\theta, \phi) = \sin \theta \cos \phi \sin \theta_B \cos \phi_B + \sin \theta \sin \phi \sin \theta_B \sin \phi_B + \cos \theta \cos \theta_B, \quad (\text{A10})$$

where the polar axis (z) is perpendicular to the microstrip surface and $\phi = 0$ is the direction of the MW magnetic field vector (x) for MW propagating along the microstrip axis (y). The ODMR spectrum is a function of the direction of the applied magnetic field. By symmetry, under hydrostatic conditions, the ODMR spectrum for a layer of random oriented NVND is only a function of the angle between applied field B and the MW field B_{MW} . The spectrum when the applied magnetic field is in the y - z plane ($\phi_B = \pi/2$), perpendicular to the MW magnetic field, is independent of θ_B and is the same as for the axially symmetric case with the magnetic field in the z direction. In this case, Eq. (A10) reduces to $n_B = \cos \theta$, and Eq. (A6) reduces to

$$S(v) = 2\pi A \int_0^\infty d\chi \int_0^{\pi/2} f_L f_{Ep} (1 + \cos^2 \theta) \sin \theta d\theta. \quad (\text{A11})$$

With the applied magnetic field perpendicular to the MW magnetic field, the spectrum becomes broader and flatter as the applied magnetic field increases, but with a steep drop at each end of the band, as shown in Fig. 6(a) and 10. As the applied field direction becomes parallel to the MW field direction, the intensity peaks that were near the ends of the band move toward the center, as shown in Fig. 10. Although the maximum splitting is produced by the NV

centers aligned with the applied field direction, intensity redistribution occurs when the contribution of these NV centers to the signal vanishes as the applied field direction becomes parallel to the MW field direction. Experimental spectra similar to those in Fig. 6(a) and 10 are compared with calculated ODMR spectra in Fig. 10(b). The parameters determining the calculated spectrum are the zero field center frequency v_D , the Lorentzian width v_L , the electric field frequency scale v_E , the applied magnetic field Zeeman shift v_B , the ^{14}N hyperfine frequency v_I (2.16 MHz), the magnetic field direction θ_B, ϕ_B , and instrumental intensity factor A . The parameters $A, v_D = 2870.8$ MHz, $v_L = 3.10$ MHz, and $v_E = 2.64$ MHz are determined by fitting Eq. (A11) to the zero field data in Fig. 10(b). The curves for $B = 15$ G in Fig. 10(b) are calculated from Eq. (A6) or Eq. (A11) using these parameter values and $v_B = 42$ MHz. The calculation satisfactorily accounts for the main features of the observed spectra, and the discrepancies could be due to small frequency dependent variations of the delivered MW power at the probe position. The magnetic field is most reliably determined from the steep outer edges of the spectrum obtained with the applied field perpendicular to the MW field. This is the basis for simple magnetic field determination from the measured ODMR spectral width using Eq. (1). He used as the PTM in the DAC solidifies at 11.8 GPa at 298 K.³⁴ Quasi-hydrostatic stress in the DAC above 12 GPa is the result of low shear strength for the He PTM, with shear strength k (GPa) = $0.008(P - P_s) + 0.00004(P - P_s)^2$ measured for He, where $P_s = 11.8$ GPa is the He solidification pressure.^{34,53} This expression gives He shear strength about 0.16 GPa at 30 GPa pressure. The uniaxial stress S in the PTM in the DAC is \leq the uniaxial yield stress for plastic flow, which is about 2 times the shear strength. The ODMR spectrum for the NVND sensor with hydrostatic pressure applied is shifted but has the same width as the ambient pressure spectrum. Uniaxial stress S broadens the ODMR spectrum due to the NV orientation dependence of the stress shift and splitting in Eqs. (A8) and (A9). Uniaxial stress $S = 0.3$ GPa in the He PTM at 30 GPa would broaden the ambient pressure ODMR peak by 0.7 MHz. The broadening of the ODMR spectrum shown in Fig. 7(b) is much larger than expected for He PTM. Figure 11 compares observed and calculated ODMR spectra. The 0 GPa curve shown in Fig. 11(a) is the curve fit to the observed ambient pressure ODMR spectrum for the 2 μm NVND layer in Fig. 7(b), using Eq. (A6) with parameters $v_L = 2.97$ MHz, $v_E = 2.23$ MHz, and $S = 0$ GPa. The other curves in Fig. 11(a) are calculated using Eq. (A6) with the ambient pressure values for v_L and v_E and successively larger values of stress S . The calculation with $S = 2.5$ GPa produces an ODMR spectrum that has the same 49 MHz width as the observed 30 GPa spectrum for the 2 μm NVND layer, but the calculated spectrum is asymmetric with three maxima, unlike the observed smooth nearly symmetric peak that is shown in Fig. 11(b). A better fit to the observed peak can be obtained using Eq. (A6) with $S = 0$, by adjusting the parameters v_L and v_E . The fit curve obtained with $v_L = 10.83$ MHz, $v_E = 4.26$ MHz, and $S = 0$ is a good fit to the observed 30 GPa spectrum, as shown in Fig. 11(b), but there is no clear physical basis for these fit parameters.

The excess broadening can be explained instead as the result of contact forces between jammed particles in the random packed NVND layer, producing large random non-uniform stress in each NVND particle.⁵⁴ The normal force between jammed particles in an isotropically compressed system has a wide distribution about the mean, with probability going to zero for small forces and probability

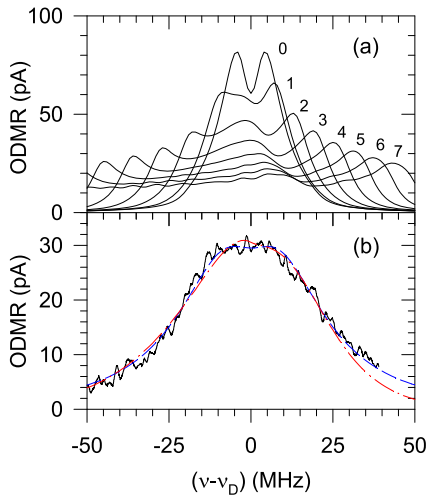


FIG. 11. (a) Calculated ODMR spectra for a NVND layer with uniform uniaxial stress $S = 0\text{--}7$ GPa. (b) The ODMR spectrum observed for a $2\ \mu\text{m}$ NVND layer at 30 GPa (black curve) is compared with the fit using effective ν_L and ν_E (blue dashed curve), and the weighted sum of spectra from (a) for a random stress distribution (red dashed-dotted curve).

decreasing exponentially for large forces.⁵⁴ A random distribution of stress magnitude S for jammed NVND particles that is qualitatively similar to the force distribution observed in Ref. 54 is $p(S) \propto (S/S_m) \exp[-(S/S_m)^{3/2}]$. Figure 11(b) shows the spectrum calculated as the weighted sum of spectra for stress S using this probability distribution as the weight factor. The stress distribution with $S_m = 3.0$ GPa which peaks at $S = (2/3)^{1/2} S_m = 2.45$ GPa gives a good fit to the observed spectrum except for the high frequency tail. Random stress S broadens the ODMR peak but does not change the mean frequency. For particles with randomly oriented uniaxial stress S , the ODMR frequency shift given by Eq. (A3) has a skew distribution with average $\langle D^S \rangle = (2\alpha_1 + \beta_1)P = 14.7P$ and width $(3/4)(\alpha_1 - \beta_1)S = 8.3S$ (FWHM), while the splitting given by Eqs. (A4) and (A5) has orientation average $\langle (E_x^S)^2 + (E_y^S)^2 \rangle = (6\alpha_2^2 + 8\beta_2^2)S^2/15 = (5.7S)^2$ and is symmetric. The random stress distribution for jammed NVND particles results in a nearly symmetric spectrum that can be fit using ambient pressure parameters ν_L , ν_E and a distribution for S (or using effective parameters ν_L and ν_E with $S = 0$). Random stress in compressed jammed NVND particles is inconsistent with hydrostatic stress exerted by He infiltrating the layer. He has been observed to solidify in contact with nanoscale charged or uncharged particles,⁵⁵ so the He infiltrating the NVND layer may be a soft solid even below 12 GPa. In this case, the NVND layer is a granular composite of hard NVND particles with soft solid He as the matrix, which is compressed by the fluid or solid He above. Broadening that increases with layer thickness and pressure, as seen in Fig. 7(b), can result because the fraction of the PTM pressure that compresses the layer increases with layer thickness, and the stress in the jammed particles increases with pressure compressing the layer. ODMR spectral broadening by random stress is smaller for a thinner NVND layer. Stress peaking at $S = 1.0$ GPa can account for the ODMR broadening for the $0.5\ \mu\text{m}$

layer at 32 GPa in Fig. 7(b). The ODMR center frequency measured at nine positions across this NVND layer at 32 GPa has a standard deviation of 2.7 MHz. The corresponding pressure variation in the DAC is 0.18 GPa, consistent with the shear strength of the He PTM at this pressure, indicating a nearly hydrostatic PTM above the NVND layer. The relatively small broadening for the $0.5\ \mu\text{m}$ NVND layer at 32 GPa may be the combined effect of stress and actual changes in ν_L and ν_E . The homogeneous width ν_L is a function of the spin relaxation rate, MW power broadening, and the light narrowing effect.^{47,48} For 0.1 W MW power producing $B_{MW} = 0.2$ G in the microstrip, the Rabi frequency is 0.3 MHz. From previous experiments with 12 ppm NV^- diamond, for 0.3 MHz Rabi frequency, the width ν_L decreases from 5 MHz at low pump light intensity to $\nu_L = 2$ MHz at high intensity.⁴⁸ The results in Fig. 7(b) use intermediate pump intensity about $10\ \text{kW}/\text{cm}^2$, which produces $\nu_L \approx 3$ MHz at ambient pressure. Assuming that decreased absorption and decreased pump rate produce the observed 20% decrease in fluorescence at 32 GPa for the $0.5\ \mu\text{m}$ NVND layer, Eq. (6) in Ref. 48 predicts an increase by 0.2 MHz for ν_L . This change in ν_L accounts for <2% of the broadening at 32 GPa.

REFERENCES

- Y. Xu, W. Zhang, and C. Tian, "Recent advances on applications of NV^- magnetometry in condensed matter physics," *Photonics Res.* **11**, 393–412 (2023).
- J. F. Barry, J. M. Schloss, E. Bauch, M. J. Turner, C. A. Hart, L. M. Pham, and R. L. Walsworth, "Sensitivity optimization for NV-diamond magnetometry," *Rev. Mod. Phys.* **92**, 015004 (2020).
- E. V. Levine, M. J. Turner, P. Kehayias, C. A. Hart, N. Langellier, R. Trubko, D. R. Glenn, R. R. Fu, and R. L. Walsworth, "Principles and techniques of the quantum diamond microscope," *Nanophotonics* **8**, 1945–1973 (2019).
- E. Abe and K. Sasaki, "Tutorial: Magnetic resonance with nitrogen-vacancy centers in diamond—microwave engineering, materials science, and magnetometry," *J. Appl. Phys.* **123**, 161101 (2018).
- M. W. Doherty, N. B. Manson, P. Delaney, F. Jelezko, J. Wrachtrup, and L. C. L. Hollenberg, "The nitrogen-vacancy colour centre in diamond," *Phys. Rep.* **528**, 1–45 (2013).
- V. M. Acosta, "Optical magnetometry with nitrogen-vacancy centers in diamond," Ph.D. dissertation (University of California, Berkeley, 2011).
- J.-H. Dai, Y. X. Shang, Y. H. Yu, Y. Xu, H. Yu, F. Hong, X. H. Yu, X. Y. Pan, and G. Q. Liu, "Optically detected magnetic resonance of diamond nitrogen-vacancy centers under megabar pressures," *Chin. Phys. Lett.* **39**, 117601 (2022).
- M. Block, B. Kobrin, A. Jarmola, S. Hsieh, C. Zu, N. L. Figueroa, V. M. Acosta, J. Minguzzi, J. R. Maze, D. Budker, and N. Y. Yao, "Optically enhanced electric field sensing using nitrogen-vacancy ensembles," *Phys. Rev. Appl.* **16**, 024024 (2021).
- T. Mittiga, S. Hsieh, C. Zu, B. Kobrin, F. Machado, P. Bhattacharyya, N. Z. Rui, A. Jarmola, S. Choi, D. Budker, and N. Y. Yao, "Imaging the local charge environment of nitrogen-vacancy centers in diamond," *Phys. Rev. Lett.* **121**, 246402 (2018).
- P. Jamonneau, M. Lesik, J. P. Tetienne, I. Alvizu, L. Mayer, A. Dreau, S. Kosen, J.-F. Roch, S. Pezzagna, J. Meijer, T. Teraji, Y. Kubo, P. Bertet, J. R. Maze, and V. Jacques, "Competition between electric field and magnetic field noise in the decoherence of a single spin in diamond," *Phys. Rev. B* **93**, 024305 (2016).
- X.-D. Chen, C.-H. Dong, F.-W. Sun, C.-L. Zou, J.-M. Cui, Z.-F. Han, and G.-C. Guo, "Temperature dependent energy level shifts of nitrogen-vacancy centers in diamond," *Appl. Phys. Lett.* **99**, 161903 (2011).
- M. W. Doherty, V. V. Struzhkin, D. A. Simpson, L. P. McGuinness, Y. Meng, A. Stacey, T. J. Karle, R. J. Hemley, N. B. Manson, L. C. L. Hollenberg, and S. Praver, "Electronic properties and metrology applications of the diamond NV^- center under pressure," *Phys. Rev. Lett.* **112**, 047601 (2014).
- L. G. Steele, M. Lawson, M. Onyszczak, B. T. Bush, Z. Mei, A. P. Dioguardi, J. King, A. Parker, A. Pines, S. T. Weir, W. Evans, K. Visbeck, Y. K. Vohra, and N. J. Curro, "Optically detected magnetic resonance of nitrogen vacancies in a

- diamond anvil cell using designer diamond anvils," *Appl. Phys. Lett.* **111**, 221903 (2017).
- ¹⁴K. O. Ho, M. Y. Leung, Y. Jiang, K. P. Ao, W. Zhang, K. Y. Yip, Y. Y. Pang, K. C. Wong, S. K. Goh, and S. Yang, "Probing local pressure environment in anvil cells with nitrogen-vacancy (NV⁻) centers in diamond," *Phys. Rev. Appl.* **13**, 024041 (2020).
- ¹⁵K. O. Ho, M. Y. Leung, W. Wang, J. Xie, K. Y. Yip, J. Wu, S. K. Goh, A. Denisenko, J. Wrachtrup, and S. Yang, "Spectroscopic study of N-V sensors in diamond-based high-pressure devices," *Phys. Rev. Appl.* **19**, 044091 (2023).
- ¹⁶S. Hsieh, P. Bhattacharyya, C. Zu, T. Mittiga, T. J. Smart, F. Machado, B. Kobrin, T. O. Hohn, N. Z. Rui, M. Kamrani, S. Chatterjee, S. Choi, M. Zaletel, V. V. Struzhkin, J. E. Moore, V. I. Levitas, R. Jeanloz, and N. Y. Yao, "Imaging stress and magnetism at high pressures using a nanoscale quantum sensor," *Science* **366**, 1349–1354 (2019).
- ¹⁷K. Y. Yip, K. O. Ho, K. Y. Yu, Y. Chen, W. Zhang, S. Kasahara, Y. Mizukami, T. Shibauchi, Y. Matsuda, S. K. Goh, and S. Yang, "Measuring magnetic field texture in correlated electron systems under extreme conditions," *Science* **366**, 1355–1359 (2019).
- ¹⁸M. Lesik, T. Plisson, L. Toraille, J. Renaud, F. Occelli, M. Schmidt, O. Salord, A. Delobbe, T. Debuisschert, L. Rondin, P. Loubeyre, and J.-F. Roch, "Magnetic measurements on micrometer-sized samples under high pressure using designed NV centers," *Science* **366**, 1359–1362 (2019).
- ¹⁹Y.-X. Shang, F. Hong, J.-H. Dai, Hui-Yu, Y.-N. Lu, E.-K. Liu, X.-H. Yu, G.-Q. Liu, and X.-Y. Pan, "Magnetic sensing inside a diamond anvil cell via nitrogen-vacancy center spins," *Chin. Phys. Lett.* **36**, 086201 (2019).
- ²⁰A. Hilberer, L. Toraille, C. Dailledouze, M.-P. Adam, L. Hanlon, G. Weck, M. Schmidt, P. Loubeyre, and J.-F. Roch, "Enabling quantum sensing under extreme pressure: Nitrogen-vacancy magnetometry up to 130 GPa," *Phys. Rev. B* **107**, L220102 (2023).
- ²¹P. Bhattacharyya, W. Chen, X. Huang, S. Chatterjee, B. Huang, B. Kobrin, Y. Lyu, T. J. Smart, M. Block, E. Wang, Z. Wang, W. Wu, S. Hsieh, H. Ma, S. Mandyam, B. Chen, E. Davis, Z. M. Geballe, C. Zu, V. Struzhkin, R. Jeanloz, J. E. Moore, T. Cui, G. Galli, B. I. Halperin, C. R. Laumann, and N. Y. Yao, "Imaging the Meissner effect in hydride superconductors using quantum sensors," *Nature* **627**, 73–79 (2024).
- ²²V. Yaroshenko, V. Soshenko, V. Vorobyov, S. Bolshedvorskii, E. Nenasheva, I. Kotelnikov, A. Akimov, and P. Kapitanova, "Circularly polarized microwave antenna for nitrogen vacancy centers in diamond," *Rev. Sci. Instrum.* **91**, 035003 (2020).
- ²³J. Herrmann, M. A. Appleton, K. Sasaki, Y. Monnai, T. Teraji, K. M. Itoh, and E. Abe, "Polarization- and frequency-tunable microwave circuit for selective excitation of nitrogen-vacancy spins in diamond," *Appl. Phys. Lett.* **109**, 183111 (2016).
- ²⁴M. Mrozek, J. Mlynarczyk, D. S. Rudnicki, and W. Gawlik, "Circularly polarized microwaves for magnetic resonance study in the GHz range: Application to nitrogen-vacancy in diamonds," *Appl. Phys. Lett.* **107**, 013505 (2015).
- ²⁵J. D. Jackson, *Classical Electrodynamics*, 3rd ed. (Wiley, 1999), Chap. 5.13, 8.1, 9.5.C, pp. 203–206, 352–356, 424.
- ²⁶R. D. Deegan, O. Bakajin, T. F. Dupont, G. Huber, S. R. Nagel, and T. A. Witten, "Capillary flow as the cause of ring stains from dried liquid drops," *Nature* **389**, 827–829 (1997).
- ²⁷H. Hu and R. G. Larson, "Marangoni effect reverses coffee-ring depositions," *J. Phys. Chem. B* **110**, 7090–7094 (2006).
- ²⁸Y. Li, Q. Yang, M. Li, and Y. Song, "Rate-dependent interface capture beyond the coffee-ring effect," *Sci. Rep.* **6**, 24628 (2016).
- ²⁹L. Bansal, P. Seth, B. Murugappan, and S. Basu, "Suppression of coffee ring: (particle) size matters," *Appl. Phys. Lett.* **112**, 211605 (2018).
- ³⁰K. N. Al-Milaji and H. Zhao, "New perspective of mitigating the coffee-ring effect: Interfacial assembly," *J. Phys. Chem. C* **123**, 12029–12041 (2019).
- ³¹H. Uchiyama, S. Saijo, S. Kishimoto, J. Ishi-Hayase, and Y. Ohno, "Operando analysis of electron devices using nanodiamond thin films containing nitrogen-vacancy centers," *ACS Omega* **4**, 7459–7466 (2019).
- ³²G. Shen, Y. Wang, A. Dewaele, C. Wu, D. E. Fratanduono, J. Eggert, S. Klotz, K. F. Dziubek, P. Loubeyre, O. V. Fat'yanov, P. D. Asimow, T. Mashimo, and R. M. M. Wentzcovitch, "Toward an international practical pressure scale: A proposal for an IPPS ruby gauge (IPPS-Ruby2020)," *High Pressure Res.* **40**, 299–314 (2020).
- ³³F. Datchi, A. Dewaele, P. Loubeyre, R. Letoullec, Y. Le Godec, and B. Canny, "Optical pressure sensors for high-pressure-high-temperature studies in a diamond anvil cell," *High Pressure Res.* **27**, 447–463 (2007).
- ³⁴K. Takemura, "Hydrostaticity in high pressure experiments: Some general observations and guidelines for high pressure experimenters," *High Pressure Res.* **41**, 155–174 (2021).
- ³⁵D. L. A. de Faria, S. Venâncio Silva, and M. T. de Oliveira, "Raman microspectroscopy of some iron oxides and oxyhydroxides," *J. Raman Spectrosc.* **28**, 873–878 (1997).
- ³⁶O. N. Shebanova and P. Lazor, "Raman spectroscopic study of magnetite (FeFe₂O₄): A new assignment for the vibrational spectrum," *J. Solid State Chem.* **174**, 424–430 (2003).
- ³⁷P. Loubeyre, R. LeToullec, J. P. Pinceaux, H. K. Mao, J. Hu, and R. J. Hemley, "Equation of state and phase diagram of solid ⁴He from single-crystal x-ray diffraction over a large P-T domain," *Phys. Rev. Lett.* **71**, 2272–2275 (1993).
- ³⁸R. L. Mills, D. H. Liebenberg, and J. C. Bronson, "Equation of state and melting properties of ⁴He from measurements to 20 kbar," *Phys. Rev. B* **21**, 5137–5147 (1980).
- ³⁹D. J. Dunstan, "Theory of the gasket in diamond anvil high-pressure cells," *Rev. Sci. Instrum.* **60**, 3789–3795 (1989).
- ⁴⁰A. Dewaele, J. H. Eggert, P. Loubeyre, and R. LeToullec, "Measurement of refractive index and equation of state in dense He, H₂, H₂O, and Ne under high pressure in a diamond anvil cell," *Phys. Rev. B* **67**, 094112 (2003).
- ⁴¹A. Dewaele, P. Loubeyre, F. Occelli, M. Mezouar, P. I. Dorogokupets, and M. Torrent, "Quasihydrostatic equation of state of iron above 2 Mbar," *Phys. Rev. Lett.* **97**, 215504 (2006).
- ⁴²N. Hirao, Y. Akahama, and Y. Ohishi, "Equations of state of iron and nickel to the pressure at the center of the earth," *Matter Radiat. Extremes* **7**, 038403 (2022).
- ⁴³J. Crangle and G. M. Goodman, "The magnetization of pure iron and nickel," *Proc. R. Soc. London, Ser. A* **321**, 477–491 (1971).
- ⁴⁴J. A. Osborn, "Demagnetizing factors of the general ellipsoid," *Phys. Rev.* **67**, 351–357 (1945).
- ⁴⁵R. Prozorov and V. G. Kogan, "Effective demagnetizing factors of diamagnetic samples of various shapes," *Phys. Rev. Appl.* **10**, 014030 (2018).
- ⁴⁶I. V. Fedotov, L. V. Doronina-Amitonova, D. A. Sidorov-Biryukov, N. A. Safronov, A. O. Levchenko, S. A. Zibrov, S. Blakley, E. Perez, A. V. Akimov, A. B. Fedotov, P. Hemmer, K. Sakoda, V. L. Velichansky, M. O. Scully, and A. M. Zheltikov, "Fiber-optic magnetometry with randomly oriented spins," *Opt. Lett.* **39**, 6755–6758 (2014).
- ⁴⁷A. Dreau, M. Lesik, L. Rondin, P. Spinicelli, O. Arcizet, J.-F. Roch, and V. Jacques, "Avoiding power broadening in optically detected magnetic resonance of single NV defects for enhanced dc magnetic field sensitivity," *Phys. Rev. B* **84**, 195204 (2011).
- ⁴⁸K. Jensen, V. M. Acosta, A. Jarmola, and D. Budker, "Light narrowing of magnetic resonances in ensembles of nitrogen-vacancy centers in diamond," *Phys. Rev. B* **87**, 014115 (2013).
- ⁴⁹S. Klotz, J.-C. Chervin, P. Munsch, and G. Le Marchand, "Hydrostatic limits of 11 pressure transmitting media," *J. Phys. D Appl. Phys.* **42**, 075413 (2009).
- ⁵⁰M. S. J. Barson, P. Peddibhotla, P. Ovarthaiyapong, K. Ganesan, R. L. Taylor, M. Gebert, Z. Mielens, B. Koslowski, D. A. Simpson, L. P. McGuinness, J. McCallum, S. Prawer, S. Onoda, T. Ohshima, A. C. Bleszynski Jayich, F. Jelezko, N. B. Manson, and M. W. Doherty, "Nanomechanical sensing using spins in diamond," *Nano Lett.* **17**, 1496–1503 (2017).
- ⁵¹P. Udvarhelyi, V. O. Shkolnikov, A. Gali, G. Burkard, and A. Palyi, "Spin-strain interaction in nitrogen-vacancy centers in diamond," *Phys. Rev. B* **98**, 075201 (2018).
- ⁵²M. Simanovskaia, K. Jensen, A. Jarmola, K. Aulenbacher, N. Manson, and D. Budker, "Sidebands in optically detected magnetic resonance signals of nitrogen vacancy centers in diamond," *Phys. Rev. B* **87**, 224106 (2013).
- ⁵³K. Takemura and A. Dewaele, "Isothermal equation of state for gold with a He-pressure medium," *Phys. Rev. B* **78**, 104119 (2008).
- ⁵⁴T. S. Majumdar and R. P. Behringer, "Contact force measurements and stress-induced anisotropy in granular materials," *Nature* **435**, 1079–1082 (2005).
- ⁵⁵P. Moroshkin, A. Hofer, S. Ulzega, and A. Weis, "Impurity-stabilized solid ⁴He below the solidification pressure of pure helium," *Nat. Phys.* **3**, 786–789 (2007).